

Fracture network localization preceding catastrophic failure

Jessica McBeck¹, Yehuda Ben-Zion², and Francois Renard³

¹University of Oslo

²University of Southern California

³University Joseph Fourier Grenoble

November 24, 2022

Abstract

We quantify the evolving spatial distribution of fracture networks throughout six in situ X-ray tomography triaxial compression experiments on monzonite and granite at confining stresses of 5-35 MPa. We first assess whether one dominant fracture continually grows at the expense of others by tracking the proportion of the maximum fracture volume to the total fracture volume. This metric does not increase monotonically. We next examine if the set of the largest fractures continually dominates deformation by tracking the proportion of the cumulative volume of fractures with volumes $>90^{\text{th}}$ percentile to the total fracture volume. This metric indicates that the fracture networks tend to increase in localization toward the largest set of fractures for up to 80% of the experimental time (differential stress), consistent with observations from southern California of localizing and delocalizing seismicity. Experiments with higher confining stress tend to have greater localization. To further assess the fracture networks localization, we compare the geometry of the set of the largest fractures to a plane. We find the best fit plane through the fractures with volumes $>90^{\text{th}}$ percentile immediately preceding failure, and calculate the distance between these fractures and the plane, and the r^2 score of the fractures and the plane throughout each experiment. The r^2 scores and the distance indicate greater localization in the monzonite experiments than in the granite experiments. The smaller mean grain size of the minerals in the granite may produce more sites of fracture nucleation and termination, leading to more delocalized fracture networks that deviate further from a plane. The higher applied confining stress in the monzonite experiments (25-35 MPa) relative to the granite experiments (5-10 MPa) may also contribute to the more localized fracture networks in the monzonite experiments. The evolution of the clustering the fractures toward the plane and the Gini coefficient, which measures the deviation of a population from uniformity, closely match each other. Tracking these metrics of localization also reveals that macroscopic yielding appears to occur when the rate of fracture network localization increases.

Fracture network localization preceding catastrophic failure in triaxial compression experiments on rocks

1 Jessica McBeck¹, Yehuda Ben-Zion², François Renard^{1,3}

2

3 ¹The Njord Centre, Departments of Geosciences and Physics, University of Oslo, Oslo,
4 Norway.

5 ²Department of Earth Sciences and Southern California Earthquake Center, University of
6 Southern California, Los Angeles, CA, USA.

7 ³University Grenoble Alpes, University Savoie Mont Blanc, CNRS, IRD, ISTERRE, Grenoble,
8 France

9 * **Correspondence:**

10 Jessica McBeck

11 j.a.mcbeck@geo.uio.no

12

13 **Key words:** fractures₁, localization₂, X-ray tomography₃, crystalline rock₄, triaxial
14 compression₅

15 **Abstract**

16 We quantify the spatial distribution of fracture networks throughout six in situ X-ray
17 tomography triaxial compression experiments on crystalline rocks at confining stresses of 5-
18 35 MPa. Tracking the proportion of the cumulative volume of fractures with volumes >90th
19 percentile to the total fracture volume, $\sum v_{90}/v_{tot}$ indicates that the fracture networks tend to
20 increase in localization toward these largest fractures for up to 80% of the applied differential
21 stress. The evolution of this metric also matches the evolution of the Gini coefficient, which
22 measures the deviation of a population from uniformity. These results are consistent with
23 observations of localizing low magnitude seismicity before large earthquakes in southern
24 California. However, the proportion of the maximum fracture volume to the total fracture
25 volume does not increase monotonically. Experiments with higher confining stress tend to
26 experience greater localization. To further quantify localization, we compare the geometry of
27 the largest fractures, with volumes >90th percentile, to the best fit plane through these
28 fractures immediately preceding failure. The r^2 scores and the mean distance of the fractures
29 to the plane indicate greater localization in monzonite than in granite. The smaller mean
30 mineral diameter and lower confining stress in the granite experiments may contribute to this
31 result. Tracking these various metrics of localization reveals a close association between
32 macroscopic yielding and the acceleration of fracture network localization. Near yielding,
33 $\sum v_{90}/v_{tot}$ and the Gini coefficient increase while the mean distance to the final failure plane
34 decreases. Macroscopic yielding thus occurs when the rate of fracture network localization
35 increases.

36 **Manuscript length:** 8900 words, 12 figures, 1 table

37 **1 Introduction**

Fracture network localization preceding catastrophic failure

38 Preexisting weaknesses control how and when rocks fail because they concentrate shear and
39 tensile stresses that promote fracture propagation under relatively low differential stress (e.g.,
40 *Griffith*, 1921). These early fractures tend to propagate parallel to the maximum compression
41 direction, σ_1 , and open perpendicular to σ_3 in rocks (e.g., *Peng & Johnson*, 1972; *Moore &*
42 *Lockner*, 1995; *Wu et al.*, 2000; *Miao et al.*, 2021). Following the wing crack model of
43 fracture network development (e.g., *Brace et al.*, 1966; *Horii & Nemat-Nasser*, 1986; *Sammis*
44 *& Ashby*, 1986; *Kemeny & Cook*, 1987), the initial propagation of a fracture from an inclined
45 preexisting fracture is stable, so increasing stress must drive further propagation. Laboratory
46 observations suggest that when the length of a fracture is comparable to the interfracture
47 spacing, fractures begin to interact with each other, prompting linkage and coalescence (e.g.,
48 *Wong*, 1982; *Kranz*, 1983; *Rawling et al.*, 2002). This transition from distributed, isolated
49 fractures to coalescing, interacting, and localizing arrays of fractures is associated with a
50 transition from stable to unstable propagation (e.g., **Figure 1**). The spatial distribution of the
51 evolving fracture network thus may provide key information about the proximity of the
52 system to failure. Indeed, fracture network clustering is a key predictor of the timing of
53 catastrophic failure in triaxial compression experiments (*McBeck et al.*, 2020a). Similarly,
54 increasing localization and clustering of low magnitude seismicity preceded several $M > 7$
55 earthquakes in southern and Baja California (*Ben-Zion and Zaliapin*, 2020).

56 Field observations and laboratory experiments show how deformation can become more
57 localized toward macroscopic failure in the laboratory, and with increasing total slip and slip-
58 rate along faults in the field (e.g., *Segall & Pollard*, 1983; *Chen & Spetzler*, 1993; *Bergbauer*
59 *& Martel*, 1999; *Pachell & Evans*, 2002; *Ben-Zion & Sammis*, 2003; *Schubnel et al.*, 2003;
60 *Kattenhorn & Marshall*, 2006; *Joussineau et al.*, 2007; *Moir et al.*, 2010; *Zhao et al.*, 2018;
61 *Kandula et al.*, 2019; *Renard et al.*, 2019a, b; *McBeck et al.*, 2020a, b). Locations of acoustic
62 emissions (AEs) captured during rock deformation experiments under triaxial compression
63 loading suggest that the AEs localize from a diffuse cloud to a narrower zone with increasing
64 deformation (*Locker et al.*, 1991; *Aben et al.*, 2019). Some experiments show that AEs can
65 propagate across the rock sample, from a smaller cluster of AEs at one edge of the rock
66 sample to a system-spanning, elongate cluster (*Benson et al.*, 2007). Some clusters of AEs
67 may include a process zone and subsequent damage zone (*Lei et al.*, 2000). Tensile fracturing
68 and low b values with a few large events characterize deformation in the process zone, while
69 shear fracturing and higher b values with a greater number of larger events characterize
70 deformation in the damage zone. These laboratory observations suggest that fracture linkage
71 is the dominant form of fracture network development following macroscopic fault
72 formation. Additional analyses identify a link between b values and the spatial distribution of
73 AEs in experiments on precut granite cores that contain faults with varying degrees of
74 roughness (*Goebel et al.*, 2017). Rougher faults have more distributed AEs and higher b
75 values than smoother faults, which produce more localized deformation with larger rupture
76 areas and thus lower b values.

77 In situ X-ray tomography experiments that capture images of three-dimensional fracture
78 networks at different times provide additional evidence of deformation localization preceding
79 catastrophic failure. Observations from X-ray tomography experiments indicate that fracture
80 networks can evolve from isolated fractures that trend parallel to σ_1 , to a linked array of
81 fractures that trends oblique to σ_1 (*Zabler et al.*, 2008; *Kandula et al.*, 2019; *Renard et al.*,
82 2018, 2019a). Similar experiments on granite and other low porosity crystalline rocks show a
83 similar tendency of increasing localization toward failure: from initially distributed fractures
84 to a system-spanning fault network (*Renard et al.*, 2017, 2019b). However, some experiments
85 on these rock types do not reveal such system-spanning faults preceding macroscopic failure

Fracture network localization preceding catastrophic failure

86 (*Renard et al.*, 2019a, b; *McBeck et al.*, 2021). In these experiments, the fracture networks
87 remain relatively distributed with several large fractures, rather than one dominant system-
88 spanning fault.

89 These previous analyses did not systematically compare the varying expressions of fracture
90 network localization, and did not examine why different experiments, under varying
91 confining stresses and on different rock types, experienced varying expressions of
92 localization. Here, we quantify and compare the evolving spatial distribution of fracture
93 networks throughout six in situ X-ray tomography triaxial compression experiments on low
94 porosity crystalline rocks: granite and monzonite. We assess the idea that one dominant
95 fracture continually grows at the expense of others by tracking the proportion of the volume
96 of the maximum fracture, v_{max} , to the total fracture volume, v_{tot} , throughout each experiment.
97 We also examine if the set of the largest fractures continually dominates deformation by
98 tracking the sum of the volume of the fractures with volumes $>90^{\text{th}}$ percentile, relative to the
99 total fracture volume, $\sum v_{90}/v_{tot}$, and the Gini coefficient, which measures the deviation of a
100 population from a uniform distribution (*Gini*, 1921). To further quantify the localization of
101 the fracture networks, we compare the geometry of the set of the largest fractures to a plane.
102 We find the best fit plane through the fractures with volumes $>90^{\text{th}}$ percentile in the
103 tomogram immediately preceding failure, and then calculate the distance between these
104 fractures and the plane, and the r^2 score of the fractures and the plane. Tracking these various
105 metrics of localization reveals fundamental insights into the temporal evolution of
106 localization toward failure, including intermittent phases of delocalization, the influence of
107 confining stress and rock type on localization, and the temporal correlation between
108 macroscopic yielding and fracture network localization.

109 2 Methods

110

111 2.1 In situ X-ray tomography

112 We use the X-ray transparent triaxial deformation apparatus Hades (*Renard et al.*, 2016)
113 installed at beamline ID19 at the European Synchrotron and Radiation facility to deform the
114 rock cores. This apparatus enables acquiring X-ray tomograms of the rock core while it is
115 inside the apparatus at the applied differential stress conditions. In these experiments, we
116 apply a constant confining stress between 5 and 35 MPa (**Table 1**) using oil surrounding the
117 jacket that contains the rock core, and then increase the axial stress in steps of 0.5-5 MPa,
118 with smaller increases of axial stress closer to macroscopic failure (**Figure 2**), at ambient
119 temperature conditions. After each stress step, we acquire 1600 radiographs at 32 bytes gray
120 scale resolution of X-ray absorption while the sample is rotated over 180° within 1.5 minutes.
121 The final reconstructed tomogram contains $1600 \times 1600 \times 1600$ voxels with $6.5 \mu\text{m}/\text{voxel}$
122 spatial sampling. Due to the stress-controlled loading conditions, the rocks fail in a sudden
123 stress drop. The final scan is acquired typically within 0.5 MPa of the final failure stress. We
124 measure the axial contraction of the rock sample using the tomograms because the shortening
125 of the rock core is visible in the three-dimensional images.

126 The rock samples are cylinders 1 cm tall and 4 mm wide. We perform three experiments on
127 Westerly granite and three experiments on monzonite. Granite and monzonite are both low
128 porosity crystalline rocks dominated by quartz and feldspar. The main difference between
129 these rocks is that the mean grain size of the granite is 100-200 micrometers, while
130 monzonite has a mean grain size of 300-400 micrometers (e.g., *Aben et al.*, 2016). Each rock

131 sample was deformed without fluid, except for monzonite #4, which included 5 MPa of
132 deionized water as pore fluid pressure.

133 Each experiment includes the typical three stages of rock deformation in the brittle regime: 1)
134 an early linear phase, 2) yielding, and 3) macroscopic failure (**Figure 2**). Due to the
135 approximately linear relationship between the axial contraction and differential stress early in
136 each experiment, we may fit a line through the data to identify the yield point. We identify
137 the yield point when the data begins to diverge from the linear fit by more than 5%. Later, we
138 compare the microscopic observations of fracture network development to the timing of the
139 macroscopic yielding. The images of the X-ray tomograms of each experiment are publicly
140 available (*Renard, 2017, 2018, 2021*).

141 **2.2 Segmentation of fracture networks**

142 During the reconstruction of the radiographs to three-dimensional volumes, we applied
143 corrections to remove acquisition noise, including ring artefacts, and to smooth variations in
144 the intensity of the X-ray source during the experiment. To remove noise from the
145 reconstructed images, we preprocessed these data using the commercial image analysis
146 software AvizoFire™, including denoising the volumes using a non-local-means filter
147 (*Buades et al., 2005*).

148 The reconstructed tomograms are three-dimensional representations of the local density of
149 the material. Pores and fractures may be distinguished from the solid rock because they have
150 distinct ranges of densities. We segment the rock into solid and fractures using a standard
151 global thresholding technique. We identify the local minimum in the histogram of the gray
152 scale values of the tomogram, indicative of density, that separates the solid material from the
153 fractures and pores (**Figure S1**). We identify this minimum threshold by fitting two Gaussian
154 distributions to the two portions of the histogram that correspond to the solid material and
155 fractures. We identify the threshold between the phases at the gray scale value when the
156 second derivative of this cumulative Gaussian distribution is closest to zero. A second
157 derivative equal to zero indicates an inflection point between the two Gaussian distributions,
158 which we use as the threshold to separate the solid from the voids.

159 **2.3 Gini coefficient**

160 We use several metrics to quantify localization, including the Gini coefficient. The Gini
161 coefficient uses the Lorenz curve of a distribution to measure the deviation from a uniform
162 distribution (e.g., *Gini, 1921; Ben-Zion & Zaliapin, 2020*). The Lorenz curve shows the
163 proportion of the total amount of a population, such as fracture volume, that is included in the
164 bottom percentile of a population. The Gini coefficient is one minus twice the integral of the
165 Lorenz curve (**Figure S2**). Thus, larger Gini coefficients indicate that the total volume of the
166 fractures in a network is dominated by a few fractures, whereas lower Gini coefficients
167 indicate that the total volume is more equally distributed among all the fractures.

168 **3 Results**

169

170 **3.1 Localization toward the largest fractures**

171 To gain a general understanding of fracture network localization in these experiments, we
172 first examine the fracture networks in the final five scans before system-size failure in two

Fracture network localization preceding catastrophic failure

173 experiments (**Figure 3**). These two experiments share some fundamental similarities in
174 fracture network development preceding macroscopic failure. In the final stages of the
175 monzonite #5 experiment (**Figure 3a**), the largest fractures appear first relatively randomly
176 spread throughout the rock core. With increasing differential stress, the fractures grow in
177 volume and link with each other. In the scan immediately preceding failure, the fracture
178 network extends from the top to the bottom of the core. Similar to the monzonite #5
179 experiment, initially the fracture and pore network in the granite #2 experiment is relatively
180 diffusely distributed (**Figure 3b**). Then, with increasing differential stress, several fractures
181 propagate and coalesce to form elongated system-spanning fault networks.

182 The fracture networks in these experiments also suggest differences in the localization
183 process between rock types. In the monzonite #5 experiment, the identified fracture network
184 extends from the top to the bottom of the core, and also has a wide lateral extent,
185 perpendicular to σ_1 . In the granite #2 experiment, the largest fractures extend from the top to
186 the bottom of the core, but are more narrowly constrained in the lateral direction. Thus, the
187 fracture network appears more localized in the granite #2 experiment immediately preceding
188 failure than the monzonite #5 experiment. Next, we assess the validity of these observations
189 by quantifying the localization of the fracture networks.

190 To quantify the coalescence of the fracture networks throughout triaxial compression, we first
191 track the proportion of the maximum fracture volume to the total volume of all the fractures,
192 v_{max}/v_{tot} , in each scan acquired throughout the experiments (**Figure 4**). High v_{max}/v_{tot} indicates
193 that the largest, most volumetric, fracture in the network dominates the network. Increasing
194 v_{max}/v_{tot} indicates that the largest fracture continually dominates an increasing proportion of
195 the fracture network. Following the idea that the fracture networks coalesce into one
196 dominant fracture, v_{max}/v_{tot} should continually increase with differential stress. However, only
197 two of the experiments (monzonite #3 and granite #4) show generally increasing v_{max}/v_{tot} ,
198 with a few episodic decreases. Instead, the majority of the experiments experience
199 delocalization away from the largest fracture, with prolonged phases of decreasing v_{max}/v_{tot} .
200 The granite #1 and #2 experiments host relatively constant v_{max}/v_{tot} until near macroscopic
201 failure, and then sharp drops in v_{max}/v_{tot} . The monzonite #4 experiment also hosts a sharp drop
202 in v_{max}/v_{tot} near failure. These sharp drops indicate that many smaller fractures are
203 propagating and lengthening in the final stages preceding failure, while the largest fracture is
204 growing at a slower rate relative to the cumulative influence of all of the smaller fractures.

205 The experiments that do not host a sharp drop in v_{max}/v_{tot} near failure show either sharp
206 (monzonite #5) or more gradual (monzonite #3, granite #4) increases in v_{max}/v_{tot} following
207 yielding and preceding macroscopic failure. Thus, following yielding, the final fracture
208 network that develops in half of the experiments is dominated by the largest fracture that
209 grows at the expense of the other fractures, and likely coalesces with several of the
210 preexisting large fractures. In the other set of the experiments, the final fracture network is
211 dominated by several large fractures, and not only one.

212 The metric of localization, v_{max}/v_{tot} , reveals that fracture network development does not
213 always follow the idealized evolution of one fracture continually growing at the expense of
214 others. Rather, the rocks experience phases of delocalization away from the largest fracture,
215 as well as the localization of deformation toward it. Due to this contrasting behavior, we next
216 examine the localization of the few largest fractures, rather than only the absolute maximum.
217 We track the set of fractures with volumes $>90^{\text{th}}$ percentile of the fracture volumes in each
218 tomogram (i.e., the cumulative volume of the top 10th percentile fractures at each stress step).

Fracture network localization preceding catastrophic failure

219 We then examine the evolution of the proportion of the sum of their fracture volumes, $\sum v_{90}$,
220 to the total fracture volume, v_{tot} , with increasing differential stress. Increasing $\sum v_{90}/v_{tot}$
221 indicates increasing localization toward the largest set of fractures in the network, with
222 volumes $>90^{\text{th}}$ percentile. We also test the influence of changing this threshold, and do not
223 observe significant differences in the results.

224 In all but one of the experiments (granite #1), the largest fractures host generally increasing
225 proportions of the total fracture network throughout loading (**Figure 5**). The granite #1
226 experiment experiences only small changes in $\sum v_{90}/v_{tot}$ (**Figure 5d, g**). Several of the
227 experiments host accelerations in $\sum v_{90}/v_{tot}$ near macroscopic failure (e.g., monzonite #5,
228 granite #4, granite #2). Other experiments show more continuous increases toward failure,
229 without significant changes in the rate of $\sum v_{90}/v_{tot}$ accumulation relative to differential
230 stress (monzonite #3 and #4). The timing of macroscopic yielding and the observed
231 acceleration in $\sum v_{90}/v_{tot}$ are similar in the majority of the experiments (granite #2 and #4,
232 monzonite #4 and #5), but appear to lack a strong correlation in other experiments (e.g.,
233 monzonite #3). To test the influence of using different thresholds, we performed this analysis
234 using the 25th, 50th, and 75th percentile thresholds (**Figure S3**). This analysis shows that the
235 overall trends of $\sum v_x/v_{tot}$ when x is 25, 50 and 75 is similar to when x is 90. Although the
236 precise magnitude of $\sum v_x/v_{tot}$ decreases with increasing x , the overall trends remain
237 unchanged. In addition, the evolution of the Gini coefficient matches the evolution of
238 $\sum v_{90}/v_{tot}$ for each experiment (**Figure S4**).

239 In summary, the majority of the experiments experience increasing localization of fracture
240 development toward the largest fractures (**Figures 5, S3, S4**), and the majority of the
241 experiments experience some phases of delocalization away from the one largest fracture
242 (**Figure 4**). Thus, the fracture network that grows at the expense of the other fractures is
243 generally comprised of several fractures, rather than only the largest fracture. Counting the
244 number of the largest fractures throughout each experiment indicates that these fracture
245 networks, composed of fractures with volumes $>90^{\text{th}}$ percentile, host hundreds of fractures
246 between the yielding point and macroscopic failure (**Figure S5**).

247 To more directly compare the signals of localization with the three metrics of the Gini
248 coefficient, $\sum v_{90}/v_{tot}$, and v_{max}/v_{tot} , we now examine the differences of these metrics
249 calculated in the final and initial tomogram of each experiment (**Figure 6**). Comparing the
250 difference in v_{max}/v_{tot} indicates that four of the six experiments experience increasing
251 localization toward the largest fracture from the final to initial scan. Thus, the proportion of
252 the total fracture network contained by the largest fracture increases from the initial to the
253 final scan in four of the six experiments. All but one of the experiments (granite #1)
254 experience localization toward the largest set of fractures, as measured with $\sum v_{90}/v_{tot}$, and
255 the Gini coefficient. The outlier experiment granite #1 produces only a small decrease in
256 $\sum v_{90}/v_{tot}$ from the final to initial scan. Thus, the largest set of fractures, with volumes $>90^{\text{th}}$
257 percentile, comprises a larger proportion of the total fracture network immediately preceding
258 failure than earlier in loading.

259 The monzonite #5 and granite #4 experiments produce the largest increases in v_{max}/v_{tot} ,
260 whereas monzonite #3 and #4 produce the largest increases in $\sum v_{90}/v_{tot}$ and the Gini
261 coefficient. These experiments have higher applied confining stress than the other
262 experiments (granite #1, #2). Thus, higher confining stresses lead to larger increases in
263 localization.

Fracture network localization preceding catastrophic failure

264 The granite #1 experiment experiences the smallest absolute changes in the localization
265 metrics. The lower applied confining stress and associated shorter yielding phase of the
266 granite #1 experiment (**Figure 2**) may produce the relatively constant localization. Although
267 granite #1 and granite #2 both experience 5 MPa confining stress, granite #1 accumulates less
268 axial strain between yielding and macroscopic failure than granite #2 (**Figure 2**). This shorter
269 yielding phase suggests that the fracture networks grew relatively slowly during yielding in
270 granite #1, producing smaller changes in the axial strain, and smaller changes in the fracture
271 network localization compared to granite #2.

272 To gain further insight into the different expressions of localization in each experiment, we
273 calculate the proportion of the accumulated differential stress (i.e., time) of the experiment in
274 which the three metrics of localization show increasing localization (**Figure 7**). The
275 differential stress that the system experiences is a proxy for time because we increase the
276 differential stress in steps toward failure, and acquire an X-ray tomogram of the system after
277 each increase in differential stress. Increases in the Gini coefficient, $\sum v_{90}/v_{tot}$, and v_{max}/v_{tot}
278 indicate that the fracture network increases in localization. Thus, we calculate the proportion
279 of the applied differential stress in which each of these three metrics increase from the
280 previous scan (and thus differential stress state). For each metric, we apply a median filter
281 with a bin size of five in order to limit the influence of small perturbations, calculate the
282 slope of the median filtered data, count the number of instances of positive slope, and then
283 sum the differential stress experienced by each scan for all of the scans with a positive slope.

284 Comparing the percentage of the differential stress in which each of these metrics are
285 localizing indicates that the Gini coefficient or $\sum v_{90}/v_{tot}$ produce higher percentages than
286 v_{max}/v_{tot} in all but one of the experiments (granite #1) (**Figure 7**). Thus, the largest fractures in
287 the network are localizing for longer periods of time than the absolute largest fracture in all
288 but one experiment. Granite #1 is the only experiment in which the largest fracture dominates
289 fracture network localization, rather than the set of the top 10th percentile of the fractures.
290 This experiment increases in localization for about 80% of the time, whereas the Gini
291 coefficient and $\sum v_{90}/v_{tot}$ increase in localization for <40% of the time.

292 Using the metric that produces the largest percentages of the experimental time (typically the
293 Gini coefficient or $\sum v_{90}/v_{tot}$, none of the experiments experience localization for more than
294 80% of the time (**Figure 7**). Two of the experiments (monzonite #5, granite #2) experience
295 localization for shorter time intervals, for only about 50% and 5%. Both of these experiments
296 host extended periods of generally decreasing localization early in the experiments, and then
297 brief periods of localization immediately preceding failure (e.g., **Figure 5**). In contrast, the
298 other experiments that host significant degrees of increasing localization, in terms of
299 magnitude and time (monzonite #3, monzonite #4, granite #4), show more prolonged phases
300 of increasing localization that begin before the macroscopic yield point (**Figure 5**).

301 3.2 Localization toward the final failure plane

302 The analyses in the previous section indicate that the largest fractures in the network, with
303 volumes >90th percentile, tend to localize for up to 80% of the experimental time (**Figure 7**).
304 To examine the evolving spatial distribution of these largest fractures toward failure, we
305 compare them to the plane that represents the final fracture network immediately preceding
306 failure (e.g., **Figure 8**). We fit this plane to the fractures with volumes >90th percentile in the
307 final scan acquired preceding macroscopic failure using least squares regression in two-
308 dimensions. We fit the plane to the largest set of fractures, rather than only the largest

Fracture network localization preceding catastrophic failure

309 fracture, because the fracture networks generally localize toward the largest set of fractures
310 (**Figure 5**), rather than the largest fracture (**Figure 4**). To assess how the fracture networks
311 coalesce toward their final geometry, we examine the r^2 score of this final failure plane and
312 the largest set of fractures throughout each experiment (**Figure 9**), and the mean distance
313 between these fractures and the failure plane (**Figures 10, 11, S6**). We calculate the mean
314 distance by finding the closest distance between each large fracture and the failure plane, and
315 then finding the mean of the distances in a given scan.

316 The fit between the final failure plane and the largest fractures (r^2 score) generally increases
317 toward failure (**Figure 9**). This trend is expected because we calculate the final failure plane
318 using the largest fractures identified in the final scan. However, the fit does not increase
319 monotonically, and instead shows some phases of delocalization away from the plane. The
320 granite #4 experiment hosts the most significant of these drops, in terms of the difference
321 relative to the maximum achieved r^2 score (**Figure 9f**). The monzonite #3 experiment also
322 shows a phase of delocalization, and then stagnating r^2 scores following the macroscopic
323 yield point. Monzonite #3 is also the experiment with the fracture network that most closely
324 fits a plane in the final scan, producing the highest r^2 score (**Figure 9g**).

325 The granite experiments all show sharp increases in the r^2 score in the final few scans
326 preceding failure. These increases coincide in time with the macroscopic yield point. In
327 contrast, the monzonite experiments show more continuous increases over longer intervals of
328 differential stress. Two of the monzonite experiments reveal changes in the r^2 score near the
329 yield point: decreasing in monzonite #3 and slowing in monzonite #4. The general trends
330 observed in the r^2 score match the trends in the mean distance between each fracture and the
331 plane (**Figure S6, Figure 11**).

332 To further examine the evolving spatial distribution of the largest fractures relative to the
333 final failure plane, we compare the r^2 score and mean distance between the fractures and the
334 plane in the initial and final scans acquired in each experiment (**Figure 10**). The monzonite
335 experiments experience larger r^2 scores in the final scan, and larger increases in the r^2 score
336 than the granite experiments. Thus, the top 10th percentile largest fractures in the final scan
337 more closely match the geometry of a plane in the monzonite experiments than those in the
338 granite experiments. In addition, at the onset of loading, the largest fractures in the monzonite
339 experiments deviate more significantly from a plane than those in the granite experiments.
340 The higher confining stress applied to the monzonite experiments may contribute to the
341 greater localization of the largest fractures toward a plane in this suite of experiments.

342 Consistent with the trend in the r^2 scores, the monzonite experiments also host lower mean
343 distances between the largest fractures and the failure plane in the final scan compared to the
344 granite experiments (**Figure 10c**). The final mean distance is relatively consistent, near 200
345 voxels, for the granite experiments. Thus, the largest fractures are more tightly clustered
346 around the final failure plane in the monzonite experiments than the granite experiments. The
347 monzonite experiments also tend to host the largest changes in the mean distance. However,
348 granite #2 also produces a significant change, while monzonite #3 produces a smaller change.
349 These changes occur at least in part because the mean distance in the initial scan is larger
350 (monzonite #3) and smaller (granite #2) than the other experiments.

351 The mean distance to the final failure plane and the Gini coefficient may correlate with each
352 other. If the largest fractures coalesce from a diffuse to localized distribution, the mean
353 distance should decrease while the Gini coefficient increases. This inverse relationship

354 generally applies to these experiments (**Figure 11**). Following yielding, the Gini coefficient
355 increases while the mean distance decreases toward failure, in all but the granite #1
356 experiment (**Figure 11d**). Thus, the fracture networks coalesce from many small distributed
357 fractures to larger well-connected fractures that increasingly localize toward the largest set of
358 fractures, and their approximate failure plane.

359 4 Discussion

360

361 4.1 Fracture network domination

362 Fracture networks develop through the linkage and coalescence of fractures. In an idealized
363 system without significant mechanical heterogeneities or interaction between neighboring
364 fractures, the localization process should be monotonic (e.g., *Lyakhovsky et al.*, 2011). The
365 relationship between the fracture length and stress intensity factor (e.g., *Isida*, 1971) suggests
366 that the largest fracture in a network should grow at the expense of the others (e.g., **Figure**
367 **12a**). If fracture networks under triaxial compression follow this evolution, then the
368 proportion of the maximum fracture volume of the total fracture volume, v_{max}/v_{tot} , should
369 increase continuously toward macroscopic failure. However, the experiments show that
370 v_{max}/v_{tot} does not increase monotonically, but instead experiences phases of delocalization of
371 the fracture network away from the largest fracture (**Figure 4**). In some experiments, v_{max}/v_{tot}
372 is smaller at the end of the experiment, immediately preceding failure, than at the beginning
373 of the experiment (**Figure 6**). Only one experiment (granite #4) experiences a systematic
374 increase in v_{max}/v_{tot} with only small perturbations. Thus, the fracture network in this
375 experiment is dominated by one large fracture that grows and perhaps coalesces relatively
376 faster than the other largest fractures. In general, however, the fracture networks are not
377 dominated by the one largest fracture. The proportion of the experimental time (differential
378 stress) in which the fracture networks experience localization toward the one largest fracture
379 generally ranges from 40-70%, with two experiments hosting <20% (**Figure 8**).

380 In contrast, the experiments experience localization toward the largest set of fractures (with
381 volumes >90th percentile) for a longer period of time than toward the one largest fracture, up
382 to 80% of the applied differential stress (**Figure 8**). Tracking the proportion of the sum of the
383 volumes >90th percentile to the total fracture volume, $\sum v_{90}/v_{tot}$, shows that all of the
384 experiments host larger $\sum v_{90}/v_{tot}$ in the scan acquired immediately preceding failure than
385 in the initial scan. Moreover, $\sum v_{90}/v_{tot}$ generally increases throughout each experiment,
386 with only small episodes of delocalization (**Figure 5**). Thus, a more general description of
387 fracture network development includes the growth and coalescence of several tens or
388 hundreds of large fractures, rather than only one (e.g., **Figure 12**).

389 Using the localization metric that produces longest periods of increasing localization, the
390 experiments tend to host localization for only up to 80% of the time (**Figure 8**). Thus, the
391 fracture network does not continually localize toward the largest set of fractures, but also
392 experiences phases with only minor changes in localization and short periods of
393 delocalization. This evolution matches observations of low magnitude seismicity in southern
394 and Baja California preceding several $M > 7$ earthquakes (*Ben-Zion & Zaliapin*, 2020).

395 The evolving fracture geometry and how it interacts with fractures and other heterogeneities
396 likely triggers these episodes of delocalization. For example, a fracture may begin to grow
397 and coalesce in one portion of the rock core, but then become impeded when it propagates
398 into the stress shadow of another fracture or a mechanical heterogeneity. When this first

399 fracture arrests its growth, other large fractures may propagate and coalesce faster. Whether
400 one fault propagates or not, and thus how fault networks develop, depend on the local tensile
401 and shear stresses that develop at the fault tips (e.g., *Paterson & Wong, 2005*). These local
402 stress concentrations influence the global mechanical efficiency of the system, suggesting
403 that the efficiency of a system can predict whether a fault will propagate, and fault network
404 development in general (e.g., *Cooke & Madden, 2014*). Numerical models suggest that
405 fracture propagation will only occur when the energetic cost of propagation is lower than the
406 gain in efficiency produced by that propagation (*Del Castello & Cooke, 2007*). Following this
407 energy budget formulation, fracture propagation and subsequent slip can reduce the total
408 internal work expended in diffuse host rock deformation while increasing the frictional work
409 done against slip (e.g., *Madden et al., 2017; McBeck et al., 2018, 2019*). Thus, faults may
410 propagate and slip only when the efficiency gained by reducing off-fault deformation (the
411 decrease in internal work) is greater than the energy consumed in fracture growth and slip
412 (the increase in frictional work and work of fault propagation).

413 The precise geometry of a fracture network, and whether it is dominated by one large fracture
414 or several large fractures, has significant implications for fluid flow in the network, and the
415 relationship between porosity and permeability. If the porosity of a rock volume arises from
416 one dominant fracture, then the resulting permeability may be at the higher end of estimates.
417 Instead, if the porosity arises from several large unconnected fractures, then the permeability
418 may be lower than expected. The evolving and varying dominance of the largest fracture in
419 these experiments underscore the importance of fluid flow simulations and experimental
420 measurements when constraining permeability (e.g., *Dardis & McCloskey, 1998; Bernabé et*
421 *al., 2003; Costa, 2006; Watanabe et al., 2009; Zhao et al., 2021*).

422 4.2 Fracture network planarity

423 Tracking the similarity of the largest set of fractures to a plane with the r^2 score indicates that
424 this set of fractures does not systematically localize toward the final failure plane throughout
425 the experiment. Instead, each experiment hosts short phases of delocalization in which the r^2
426 score temporarily decreases or remains at similar values (**Figure 9**). If fracture networks
427 develop from one dominant fracture that continually grows at the expense of others (**Figure**
428 **12**), then the r^2 score may tend to increase monotonically. However, because one fracture
429 does not tend to dominate the full fracture network throughout all of the experiments, the
430 evolving geometry of the largest set of fractures does not systematically increase toward
431 planarity.

432 The planarity immediately preceding failure of the largest set of fractures, with volumes $>90^{\text{th}}$
433 percentile, differs in the experiments on granite and monzonite (**Figure 10**). The r^2 score is
434 generally higher for the monzonite experiments than for the granite experiments. Similarly,
435 the mean distance of the largest fractures to the failure plane is generally smaller for the
436 monzonite experiments than for the granite experiments. Thus, the fracture network that
437 develops immediately preceding failure in the monzonite experiments more closely matches a
438 plane than the network that develops in the granite experiments. This difference may arise
439 from the higher confining stress applied to the monzonite experiments (25-35 MPa)
440 compared to the granite experiments (5-10 MPa). The higher confining stress could promote
441 greater localization of the fracture network to a plane in the monzonite experiments. Previous
442 laboratory experiments demonstrate that higher confining stress can produce localized shear
443 failure planes, while rocks under lower confinement fail via more distributed axial splitting
444 (e.g., *Amann et al., 2012*). These laboratory results are also consistent with observations that

Fracture network localization preceding catastrophic failure

445 indicate that earthquake-induced rock damage in southern California is more localized and
446 continuous at greater depth than near the surface (*Ben-Zion & Zaliapin, 2019*).

447 The larger mean grain size of the monzonite compared to the granite could also contribute to
448 this difference in localization. Grain boundaries in crystalline rocks can influence where
449 fractures nucleate because the constitutive minerals have varying stiffness (e.g., *Tapponnier
450 & Brace, 1976; Moore & Lockner, 1995*). The material contrast produces differential
451 compaction that leads to stress concentrations. The smaller grain size in the granite could lead
452 to more sites of fracture nucleation and termination at the edges of minerals of different
453 stiffnesses than the monzonite. The resulting greater number of sites of nucleation and
454 termination could then produce more delocalized fracture networks in the granite than the
455 monzonite.

456 In most experiments, the Gini coefficient and the mean distance to the failure plane are
457 relatively constant, and then accelerate and decelerate close to macroscopic failure,
458 respectively (**Figure 11**). The timing of this change in rate occurs near or slightly before the
459 macroscopic yield point (within 10 MPa of differential stress) in some of the experiments
460 (e.g., granite #2, monzonite #4 and #5), while in others this change occurs at least 20 MPa of
461 differential stress before the yield point (e.g., granite #4). Thus, the reorganization of the
462 fracture network that includes accelerating localization toward the largest set of fractures
463 often precedes the macroscopic yield point. The acceleration of fracture network localization
464 produces increasingly larger changes in the axial contraction for equal increments of
465 differential stress. Fracture network localization may coincide in time with a transition from
466 slower to faster fracture growth (e.g., *Thompson et al., 2006*). Because we load the rock core
467 with differential stress steps, and stop increasing the differential stress to acquire a tomogram,
468 the fracture growth that we capture in the tomograms is stable, and does not occur with an
469 accelerating, unstable rate. Thus, in our experiments, the acceleration of fracture network
470 localization may coincide in time with the transition from slower to faster fracture growth.
471 Under more continuous differential stress or axial strain loading conditions, the localization
472 of the fracture network may coincide with the transition from stable to unstable fracture
473 growth. Previous work has also inferred a link between unstable fracture growth and fracture
474 coalescence (e.g., *Nicksiar & Martin, 2012*). Other work has linked the transition from quasi-
475 static to unstable fracture growth to a critical crack length (e.g., *Ohnaka & Kuwahara, 1990*).

476 5 Conclusions

477 We quantify the spatial distribution of fracture networks throughout six in situ X-ray
478 tomography triaxial compression experiments approaching system-size failure under
479 confining stress conditions of the upper crust. We assess the idea that one dominant fracture
480 continually grows at the expense of others by tracking the ratio v_{max}/v_{tot} of the largest fracture
481 volume relative to the total fracture volume throughout each experiment. The results show
482 that v_{max}/v_{tot} does not systematically increase in the experiments. We then examine if a set of
483 the largest fractures continually dominates deformation by tracking the sum of the volume of
484 the fractures with volumes $>90^{th}$ percentile relative to the total fracture volume, $\sum v_{90}/v_{tot}$.
485 This metric indicates that the fracture networks tend to increase in localization toward the
486 largest set of fractures for up to 80% of the experimental time (differential stress). The
487 evolution of this metric matches the evolution of the Gini coefficient. Experiments with
488 higher applied confining stress tend to experience greater increases in localization.

Fracture network localization preceding catastrophic failure

489 Comparing the geometry of the set of the largest fractures to a plane with the r^2 score
490 indicates that it is more similar to a plane in the monzonite experiments than the granite
491 experiments. In addition, the mean distance between the plane and the set of fractures is
492 smaller in the monzonite experiments than the granite experiments. The smaller mean grain
493 size in the granite may produce more sites of fracture nucleation and termination, leading to
494 more delocalized fracture networks that deviate further from a plane. The higher applied
495 confining stress of the monzonite experiments (25-35 MPa) relative to the granite
496 experiments (5-10 MPa) may also contribute to the more localized fracture networks in the
497 monzonite experiments. Tracking these metrics of localization reveals a close association
498 between the macroscopic yielding of the rock and the acceleration of the localization of the
499 fracture network. Near yielding, $\sum v_{90}/v_{tot}$ and the Gini coefficient increase while the mean
500 distance between the largest set of fractures and the final failure plane decreases.
501 Macroscopic yielding occurs when the rate of fracture network localization increases. The
502 macroscopic yielding may occur when the fractures begin to grow and coalesce faster,
503 producing increasingly localized fracture networks.

504 Acknowledgements

505 We thank Elodie Boller, Paul Tafforeau, and Alexander Rack for advice about the design of
506 the tomography setup, Benoît Cordonnier for the help with experiments, and Sanchez
507 Technology for building the deformation apparatus. The Research Council of Norway (grant
508 300435 to JAM) and U.S. Department of Energy (award DE-SC0016520 to YBZ) funded this
509 work. Sigma2-NIRD provided data storage (grant NS9073K). Beamtime was allocated at the
510 European Synchrotron Radiation Facility (Long Term Proposal ES-295). The experimental
511 data of time series of X-ray tomograms are available on Norstore: including the three
512 monzonite samples (Renard, 2017, 2018), and the three Westerly granite samples (Renard,
513 2021).

514 References

- 515 Aben, F. M., Brantut, N., Mitchell, T. M., & David, E. C. (2019). Rupture energetics in
516 crustal rock from laboratory-scale seismic tomography. *Geophysical Research*
517 *Letters*, 46(13), 7337-7344.
- 518 Aben, F. M., Doan, M. L., Mitchell, T. M., Toussaint, R., Reuschlé, T., Fondriest, M., ... &
519 Renard, F. (2016). Dynamic fracturing by successive coseismic loadings leads to
520 pulverization in active fault zones. *Journal of Geophysical Research: Solid Earth*, 121(4),
521 2338-2360.
- 522 Amann, F., Kaiser, P., & Button, E. A. (2012). Experimental study of brittle behavior of clay
523 shale in rapid triaxial compression. *Rock Mechanics and Rock Engineering*, 45(1), 21-33.
- 524 Buades, A., Coll, B., & Morel, J. M. (2005, June). A non-local algorithm for image
525 denoising. In 2005 IEEE Computer Society Conference on Computer Vision and Pattern
526 Recognition (CVPR'05) (Vol. 2, pp. 60-65). IEEE.
- 527 Ben-Zion, Y., & Sammis, C. G. (2003). Characterization of fault zones. *Pure and applied*
528 *geophysics*, 160(3), 677-715.
- 529 Ben-Zion, Y., & Zaliapin, I. (2019). Spatial variations of rock damage production by
530 earthquakes in southern California. *Earth and Planetary Science Letters*, 512, 184-193.
- 531 Ben-Zion, Y., & Zaliapin, I. (2020). Localization and coalescence of seismicity before large
532 earthquakes. *Geophysical Journal International*, 223(1), 561-583.

Fracture network localization preceding catastrophic failure

- 533 Bergbauer, S., & Martel, S. J. (1999). Formation of joints in cooling plutons. *Journal of*
534 *Structural Geology*, 21(7), 821-835
- 535 Bernabé, Y., Mok, U., & Evans, B. (2003). Permeability-porosity relationships in rocks
536 subjected to various evolution processes. *Pure and Applied Geophysics*, 160(5), 937-960.
- 537 Brace, W. F., Paulding Jr, B. W., & Scholz, C. H. (1966). Dilatancy in the fracture of
538 crystalline rocks. *Journal of Geophysical Research*, 71(16), 3939-3953.
- 539 Chen, G., & Spetzler, H. (1993). Complexities of rock fracture and rock friction from
540 deformation of Westerly granite. *pure and applied geophysics*, 140(1), 95-121.
- 541 Cooke, M. L., & Madden, E. H. (2014). Is the Earth lazy? A review of work minimization in
542 fault evolution. *Journal of Structural Geology*, 66, 334-346.
- 543 Costa, A. (2006). Permeability-porosity relationship: A reexamination of the Kozeny-Carman
544 equation based on a fractal pore-space geometry assumption. *Geophysical research*
545 *letters*, 33(2).
- 546 Crider, J. G. (2015). The initiation of brittle faults in crystalline rock. *Journal of Structural*
547 *Geology*, 77, 159-174.
- 548 Dardis, O., & McCloskey, J. (1998). Permeability porosity relationships from numerical
549 simulations of fluid flow. *Geophysical Research Letters*, 25(9), 1471-1474.
- 550 Del Castello, M., & Cooke, M. L. (2007). Underthrusting-accretion cycle: Work budget as
551 revealed by the boundary element method. *Journal of Geophysical Research: Solid*
552 *Earth*, 112(B12).
- 553 Gini, C. (1921). Measurement of inequality of incomes. *The economic journal*, 31(121), 124-
554 126.
- 555 Goebel, T. H., Kwiatak, G., Becker, T. W., Brodsky, E. E., & Dresen, G. (2017). What
556 allows seismic events to grow big?: Insights from b-value and fault roughness analysis in
557 laboratory stick-slip experiments. *Geology*, 45(9), 815-818.
- 558 Griffith, A. A. (1921). VI. The phenomena of rupture and flow in solids. *Philosophical*
559 *transactions of the royal society of london. Series A, containing papers of a mathematical or*
560 *physical character*, 221(582-593), 163-198.
- 561 De Jossineau, G., Mutlu, O., Aydin, A., & Pollard, D. D. (2007). Characterization of strike-
562 slip fault–splay relationships in sandstone. *Journal of Structural Geology*, 29(11), 1831-1842.
- 563 Kandula, N., Cordonnier, B., Boller, E., Weiss, J., Dysthe, D. K., & Renard, F. (2019).
564 Dynamics of microscale precursors during brittle compressive failure in Carrara
565 marble. *Journal of Geophysical Research: Solid Earth*, 124(6), 6121-6139.
- 566 Kattenhorn, S. A., & Marshall, S. T. (2006). Fault-induced perturbed stress fields and
567 associated tensile and compressive deformation at fault tips in the ice shell of Europa:
568 implications for fault mechanics. *Journal of structural geology*, 28(12), 2204-2221.
- 569 Kemeny, J. M., & Cook, N. G. (1991). Micromechanics of deformation in rocks.
570 *In Toughening mechanisms in quasi-brittle materials (pp. 155-188)*. Springer, Dordrecht.
- 571 Kranz, R. L. (1983). Microcracks in rocks: a review. *Tectonophysics*, 100(1-3), 449-480.
- 572 Horii, H., & Nemat-Nasser, S. (1986). Brittle failure in compression: splitting faulting and
573 brittle-ductile transition. *Philosophical Transactions of the Royal Society of London. Series*
574 *A, Mathematical and Physical Sciences*, 319(1549), 337-374.

Fracture network localization preceding catastrophic failure

- 575 Lei, X., Kusunose, K., Rao, M. V. M. S., Nishizawa, O., & Satoh, T. (2000). Quasi-static
576 fault growth and cracking in homogeneous brittle rock under triaxial compression using
577 acoustic emission monitoring. *Journal of Geophysical Research: Solid Earth*, 105(B3), 6127-
578 6139.
- 579 Lyakhovskiy, V., Hamiel, Y., & Ben-Zion, Y. (2011). A non-local visco-elastic damage
580 model and dynamic fracturing. *Journal of the Mechanics and Physics of Solids*, 59(9), 1752-
581 1776.
- 582 Isida, M. (1971). Effect of width and length on stress intensity factors of internally cracked
583 plates under various boundary conditions. *International Journal of Fracture Mechanics*, 7(3),
584 301-316.
- 585 Madden, E. H., Cooke, M. L., & McBeck, J. (2017). Energy budget and propagation of faults
586 via shearing and opening using work optimization. *Journal of Geophysical Research: Solid
587 Earth*, 122(8), 6757-6772.
- 588 McBeck, J. A., Aiken, J. M., Mathiesen, J., Ben-Zion, Y., & Renard, F. (2020a). Deformation
589 precursors to catastrophic failure in rocks. *Geophysical Research Letters*, 47(24),
590 e2020GL090255.
- 591 McBeck, J., Aiken, J. M., Ben-Zion, Y., & Renard, F. (2020b). Predicting the proximity to
592 macroscopic failure using local strain populations from dynamic in situ X-ray tomography
593 triaxial compression experiments on rocks. *Earth and Planetary Science Letters*, 543, 116344.
- 594 McBeck, J., Cooke, M., Souloumiac, P., Maillot, B., & Mary, B. (2018). The influence of
595 detachment strength on the evolving deformational energy budget of physical accretionary
596 prisms. *Solid Earth*, 9(6), 1421-1436
- 597 McBeck, J., Cordonnier, B., Mair, K., & Renard, F. (2019). The evolving energy budget of
598 experimental faults within continental crust: Insights from in situ dynamic X-ray
599 microtomography. *Journal of Structural Geology*, 123, 42-53.
- 600 McBeck, J. A., Zhu, W., & Renard, F. (2021). The competition between fracture nucleation,
601 propagation, and coalescence in dry and water-saturated crystalline rock. *Solid Earth*, 12(2),
602 375-387.
- 603 Miao, S., Pan, P. Z., Zhao, X., Shao, C., & Yu, P. (2021). Experimental study on damage and
604 fracture characteristics of Beishan granite subjected to high-temperature treatment with DIC
605 and AE techniques. *Rock Mechanics and Rock Engineering*, 54(2), 721-743.
- 606 Moir, H., Lunn, R. J., Shipton, Z. K., & Kirkpatrick, J. D. (2010). Simulating brittle fault
607 evolution from networks of pre-existing joints within crystalline rock. *Journal of Structural
608 Geology*, 32(11), 1742-1753.
- 609 Moore, D. E., & Lockner, D. A. (1995). The role of microcracking in shear-fracture
610 propagation in granite. *Journal of Structural Geology*, 17(1), 95-114
- 611 Paterson, M. S., & Wong, T. F. (2005). *Experimental rock deformation-the brittle field*.
612 Springer Science & Business Media.
- 613 Peng, S., & Johnson, A. M. (1972, January). Crack growth and faulting in cylindrical
614 specimens of Chelmsford granite. In *International Journal of Rock Mechanics and Mining
615 Sciences & Geomechanics Abstracts* (Vol. 9, No. 1, pp. 37-86). Pergamon.
- 616 Rawling, G. C., Baud, P., & Wong, T. F. (2002). Dilatancy, brittle strength, and anisotropy of
617 foliated rocks: Experimental deformation and micromechanical modeling. *Journal of
618 Geophysical Research: Solid Earth*, 107(B10), ETG-8

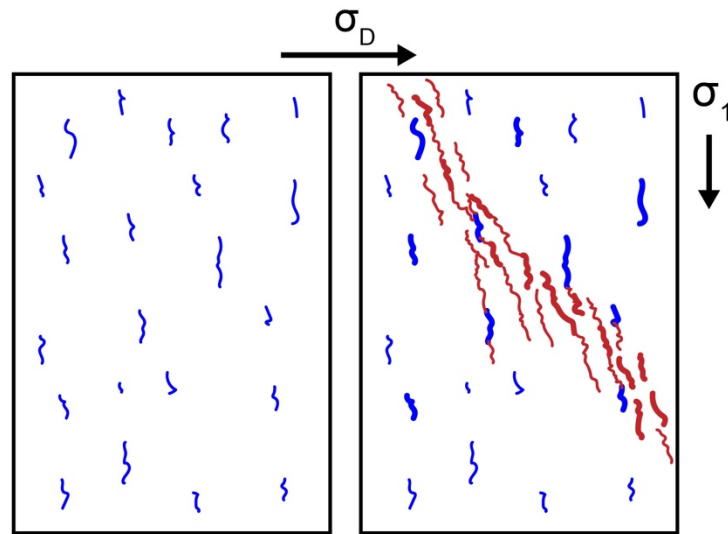
Fracture network localization preceding catastrophic failure

- 619 Renard, F. (2017). Critical evolution of damage towards system size failure in a crystalline
620 rock [Data set]. Norstore. doi:10.11582/2017.00025.
- 621 Renard, F. (2018). Volumetric and shear processes in crystalline rock during the approach to
622 faulting [Data set]. Norstore. doi:10.11582/2018.00023.
- 623 Renard, F. (2021). X-ray tomography data of Westerley granite [Data set]. Norstore.
624 doi:10.11582/2021.00002.
- 625 Renard, F., Cordonnier, B., Dysthe, D. K., Boller, E., Tafforeau, P., & Rack, A. (2016). A
626 deformation rig for synchrotron microtomography studies of geomaterials under conditions
627 down to 10 km depth in the Earth. *Journal of Synchrotron Radiation*, 23(4), 1030-1034.
- 628 Renard, F., McBeck, J., Cordonnier, B., Zheng, X., Kandula, N., Sanchez, J. R., & Dysthe, D.
629 K. (2019a). Dynamic in situ three-dimensional imaging and digital volume correlation
630 analysis to quantify strain localization and fracture coalescence in sandstone. *Pure and
631 Applied Geophysics*, 176(3), 1083-1115.
- 632 Renard, F., McBeck, J., Kandula, N., Cordonnier, B., Meakin, P., & Ben-Zion, Y. (2019b).
633 Volumetric and shear processes in crystalline rock approaching faulting. *Proceedings of the
634 National Academy of Sciences*, 116(33), 16234-16239.
- 635 Renard, F., Cordonnier, B., Kobchenko, M., Kandula, N., Weiss, J., & Zhu, W. (2017).
636 Microscale characterization of rupture nucleation unravels precursors to faulting in
637 rocks. *Earth and Planetary Science Letters*, 476, 69-78.
- 638 Renard, F., Weiss, J., Mathiesen, J., Ben Zion, Y., Kandula, N., Cordonnier, B. (2018)
639 Critical evolution of damage towards system-size failure in crystalline rock, *Journal of
640 Geophysical Research*, 123, 1969-1986.
- 641 Sammis, C. G., & Ashby, M. F. (1986). The failure of brittle porous solids under compressive
642 stress states. *Acta Metallurgica*, 34(3), 511-526.
- 643 Segall, P., & Pollard, D. D. (1983). Nucleation and growth of strike slip faults in
644 granite. *Journal of Geophysical Research: Solid Earth*, 88(B1), 555-568.
- 645 Schubnel, A., Nishizawa, O., Masuda, K., Lei, X. J., Xue, Z., & Guéguen, Y. (2003).
646 Velocity measurements and crack density determination during wet triaxial experiments on
647 Oshima and Toki granites. In *Thermo-Hydro-Mechanical Coupling in Fractured Rock* (pp.
648 869-887). Birkhäuser, Basel.
- 649 Tapponnier, P., & Brace, W.F. (1976). Development of stress-induced microcracks in
650 Westerly granite. *International Journal of Rock Mechanics and Mining Sciences &
651 Geomechanics Abstracts*, 13(4), 103-112. Pergamon.
- 652 Thompson, B. D., Young, R. P., & Lockner, D. A. (2006). Fracture in Westerly granite under
653 AE feedback and constant strain rate loading: nucleation, quasi-static propagation, and the
654 transition to unstable fracture propagation. *Pure and Applied Geophysics*, 163(5), 995-1019.
- 655 Watanabe, N., Hirano, N., & Tsuchiya, N. (2009). Diversity of channeling flow in
656 heterogeneous aperture distribution inferred from integrated experimental-numerical analysis
657 on flow through shear fracture in granite. *Journal of Geophysical Research: Solid
658 Earth*, 114(B4), B04208.
- 659 Wong, T. F. (1982). Micromechanics of faulting in Westerly granite. In *International Journal
660 of Rock Mechanics and Mining Sciences & geomechanics abstracts* (Vol. 19, No. 2, pp. 49-
661 64). Pergamon.

Fracture network localization preceding catastrophic failure

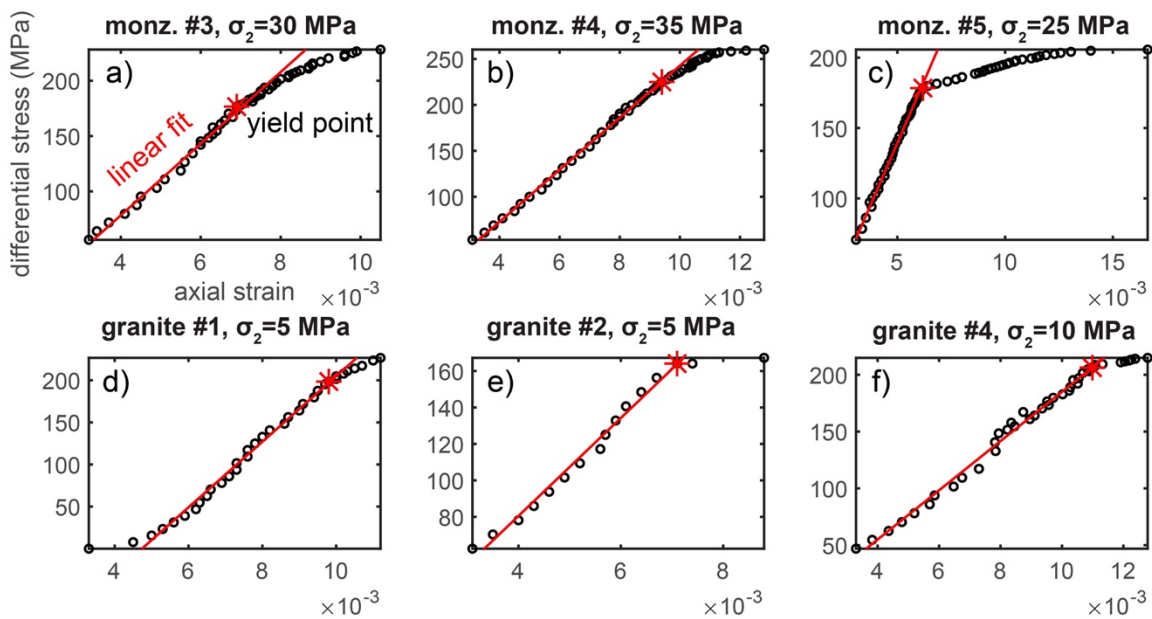
- 662 Wu, X. Y., Baud, P., & Wong, T. F. (2000). Micromechanics of compressive failure and
663 spatial evolution of anisotropic damage in Darley Dale sandstone. *International Journal of*
664 *Rock Mechanics and Mining Sciences*, 37(1-2), 143-160.
- 665 Zabler, S., Rack, A., Manke, I., Thermann, K., Tiedemann, J., Harthill, N., & Riesemeier, H.
666 (2008). High-resolution tomography of cracks, voids and micro-structure in greywacke and
667 limestone. *Journal of Structural Geology*, 30(7), 876-887.
- 668 Zhao, C., Zhou, Y., Zhao, C., & Bao, C. (2018). Cracking processes and coalescence modes
669 in rock-like specimens with two parallel pre-existing cracks. *Rock Mechanics and Rock*
670 *Engineering*, 51(11), 3377-3393.
- 671 Zhao, Z., Zhao, Y., Jiang, Z., Guo, J., and Zhang, R. (2021). Investigation of Fracture
672 Intersection Behaviors in Three-Dimensional Space Based on CT Scanning Experiments.
673 *Rock Mech Rock Eng.* <https://doi.org/10.1007/s00603-021-02587-9>.

674 **Figures**



675

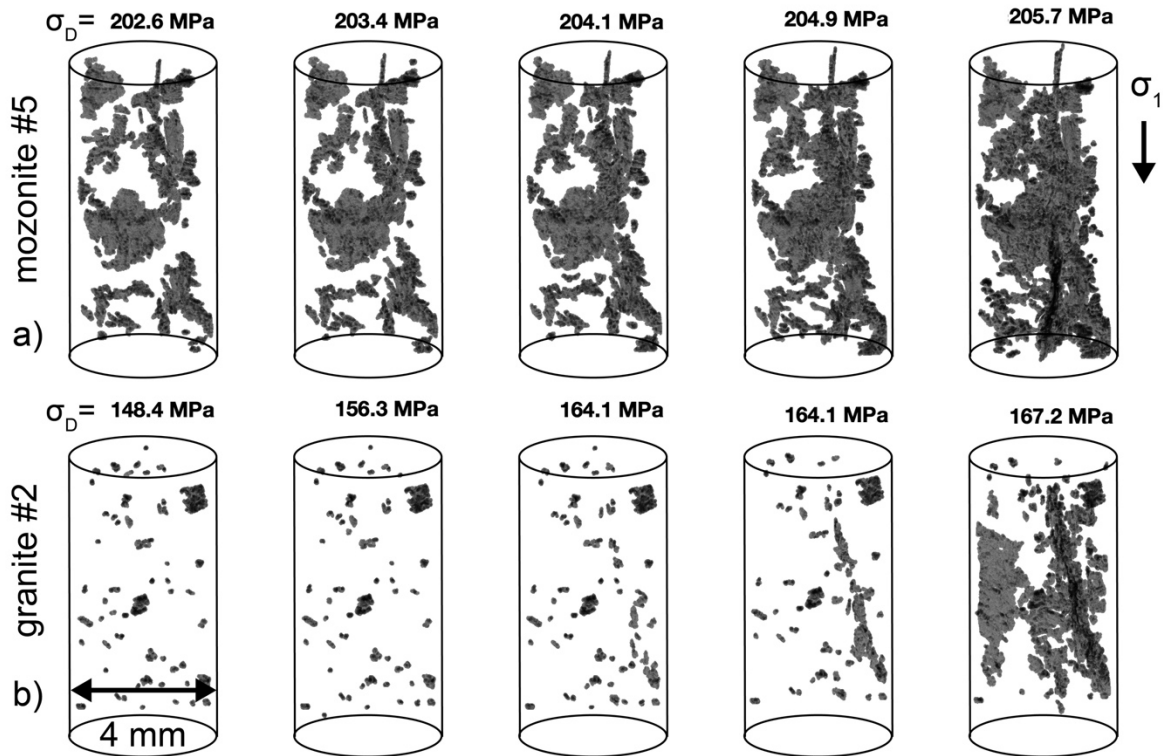
676 **Figure 1.** Transition from stable (left) to unstable (right) fracture network development via
 677 coalescence of fractures with increasing differential stress, σ_D . Left: Under lower σ_D ,
 678 microfractures nucleate and grow parallel to the main compressive stress, σ_1 . Right: With
 679 increasing σ_D , approaching system-size failure, the microfractures grow, interact, and link to
 680 form a connected fault.



681

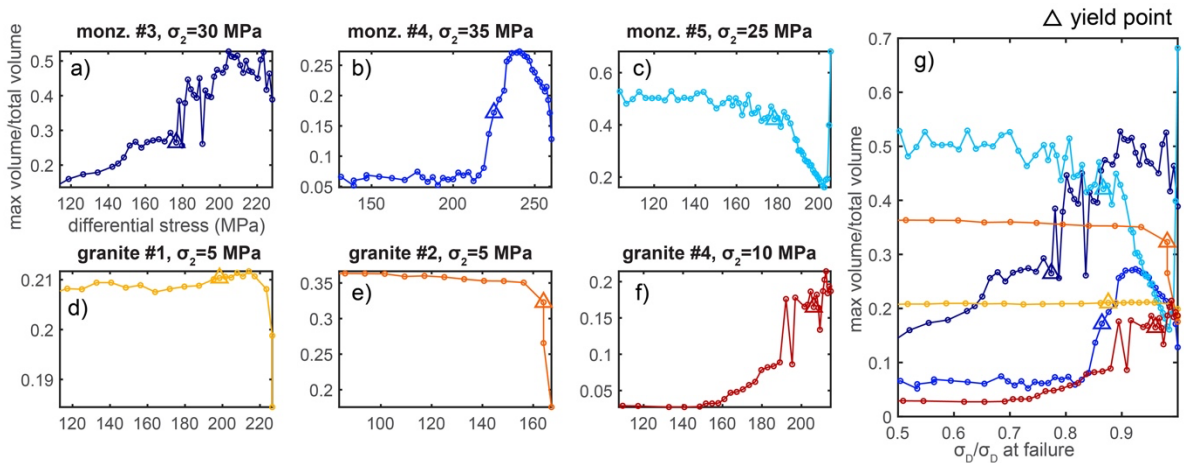
682 **Figure 2.** Differential stress versus axial strain relationships for the six examined
 683 experiments: a) monzonite #3, b) monzonite #4, c) monzonite #5, d) granite #1, e) granite #2,
 684 and f) granite #4. Black circles show the conditions when an X-ray tomogram was acquired.
 685 Red lines show the linear fit of the early portion of the data. Red stars show the identified
 686 yield point, when the data diverges from the linear fit. The title of each plot shows the
 687 experiment abbreviation (**Table 1**), and applied confining stress, σ_2 . In experiment monz. #4,
 688 we applied a pore fluid pressure, $p=5$ MPa.

Fracture network localization preceding catastrophic failure



689
690
691
692
693

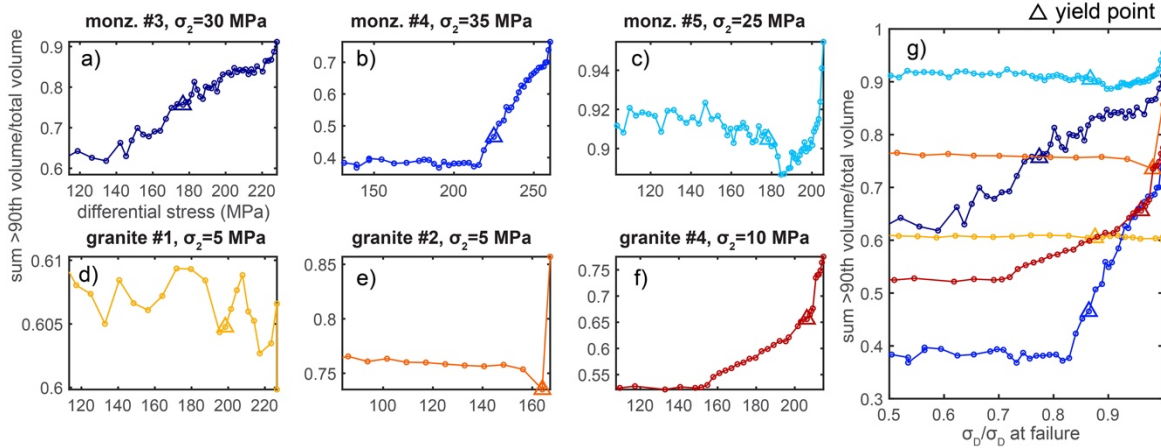
Figure 3. Fracture network development in the final five tomograms preceding macroscopic failure in experiment monzonite #5 (a) and granite #2 (b). Black regions show the fractures with volumes greater than the 90th percentile of the population. Numbers at the top of the cores show the differential stress applied on the sample when the scan was acquired.



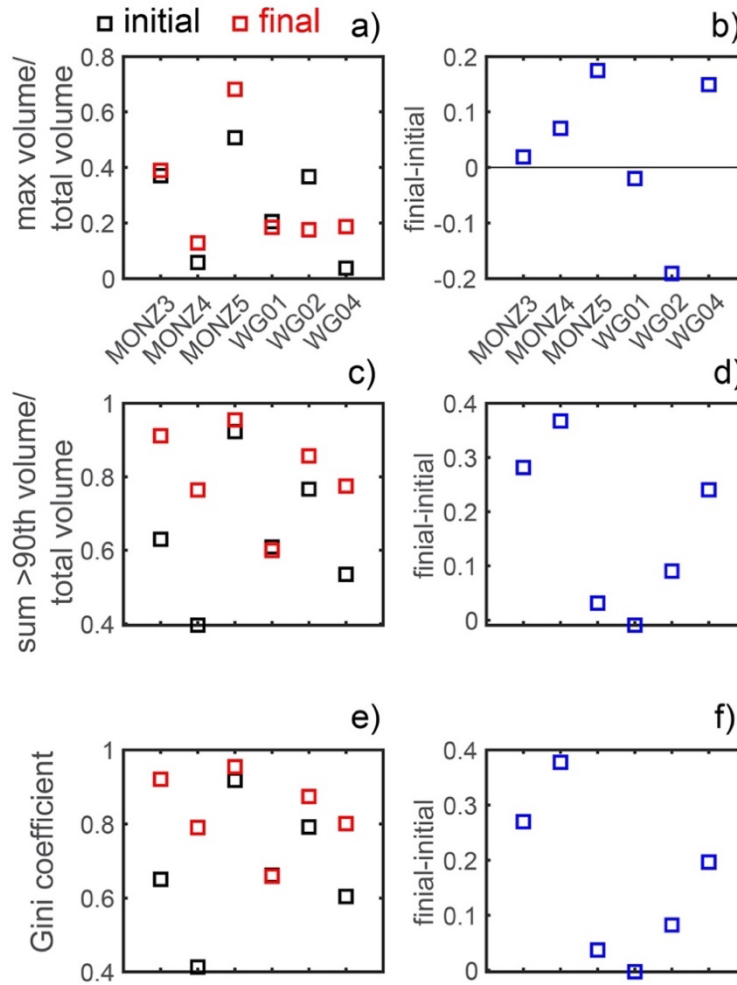
694
695
696
697
698
699

Figure 4. Evolution of the maximum fracture volume divided by the total volume of fractures, v_{max}/v_{tot} , throughout each individual experiment (a-f), and for all the experiments (g). Color of the lines in (g) matches the colors of each experiment shown in (a-f). Triangles show the conditions of the yield point. Increasing v_{max}/v_{tot} indicates that the fracture network is localizing toward the one largest fracture.

Fracture network localization preceding catastrophic failure



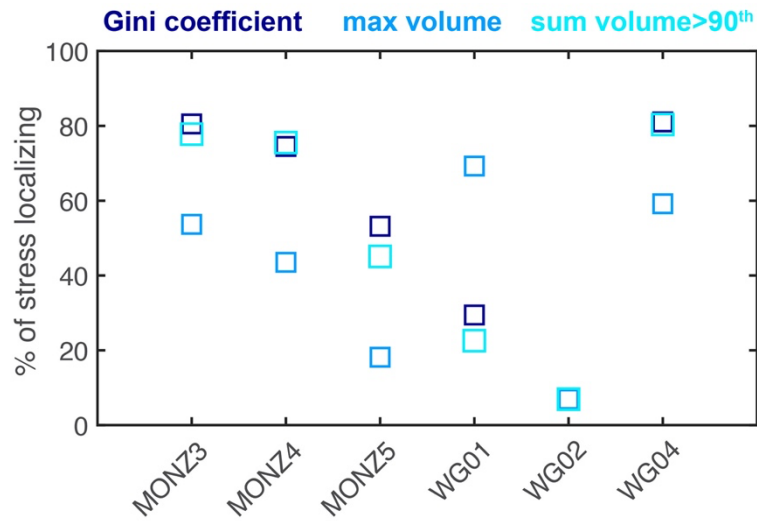
700
 701 **Figure 5.** Evolution of the sum of the fracture volumes with values $>90^{\text{th}}$ percentile divided
 702 by the total volume of fractures, $\sum v_{90}/v_{tot}$, throughout each individual experiment (a-f), and
 703 for all the experiments (g). Color of the lines in (g) matches the colors of each experiment
 704 shown in (a-f). Triangles show the conditions of the yield point. Increasing $\sum v_{90}/v_{tot}$
 705 indicates increasing localization toward the largest fractures in the network, with volumes
 706 $>90^{\text{th}}$ percentile.



707 **Figure 6.** Difference in the v_{max}/v_{tot} (a-b), $\sum v_{90}/v_{tot}$ (c-d), and the Gini coefficient (e-f) from
 708 the initial and final tomogram acquired in each experiment. Positive changes from the initial

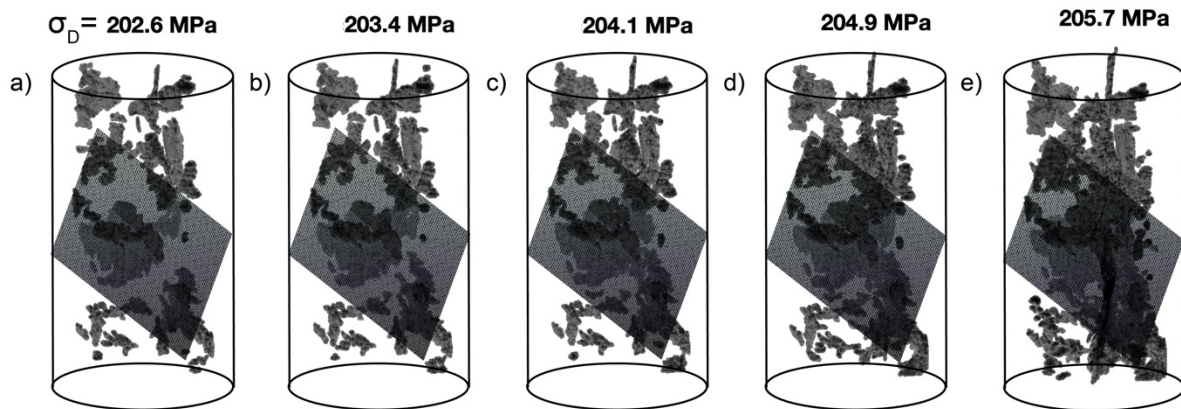
Fracture network localization preceding catastrophic failure

709 to final scan indicate increasing localization. The results of the Gini coefficient and
 710 $\sum v_{90}/v_{tot}$ are nearly identical.



711

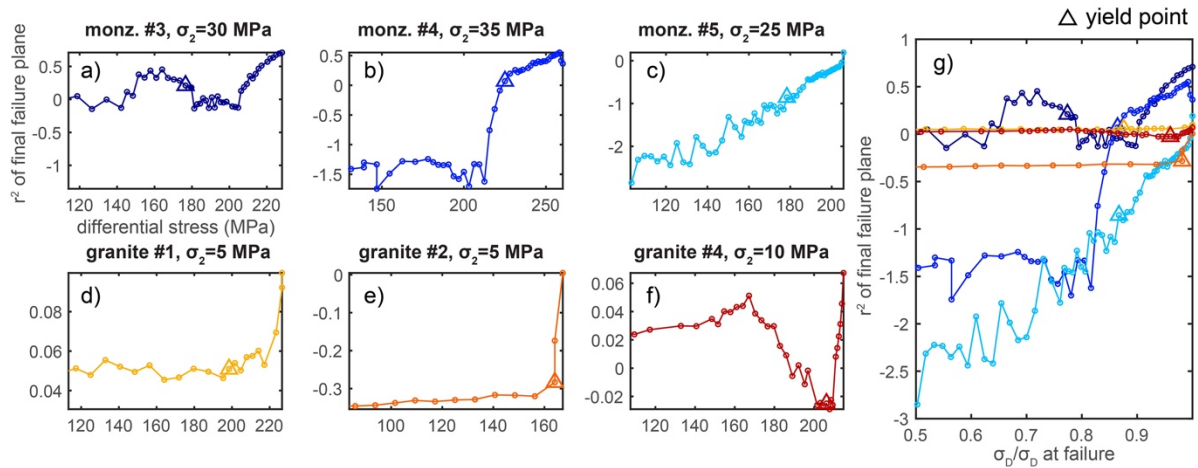
712 **Figure 7.** Percentage of the applied differential stress in which the Gini coefficient, v_{max}/v_{tot} ,
 713 and $\sum v_{90}/v_{tot}$ show localization, i.e., increase from one scan to the next.



714

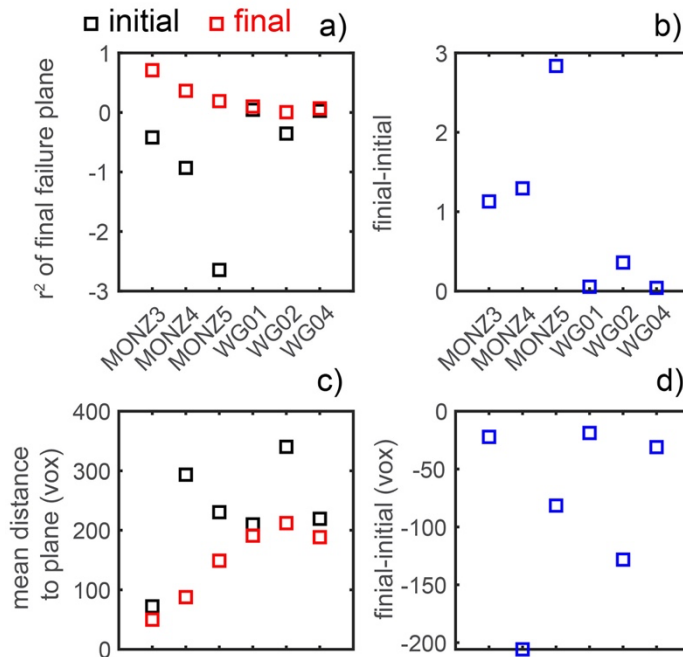
715 **Figure 8.** Largest fractures, with volumes >90th percentile, in the five scans acquired before
 716 failure in the monzonite #5 experiment, and best fit plane of the final fault geometry. The
 717 final failure plane is built from the scan acquired immediately preceding failure. Numbers at
 718 the top of the cores show the differential stress when the scan was acquired.

Fracture network localization preceding catastrophic failure



719
720
721
722
723

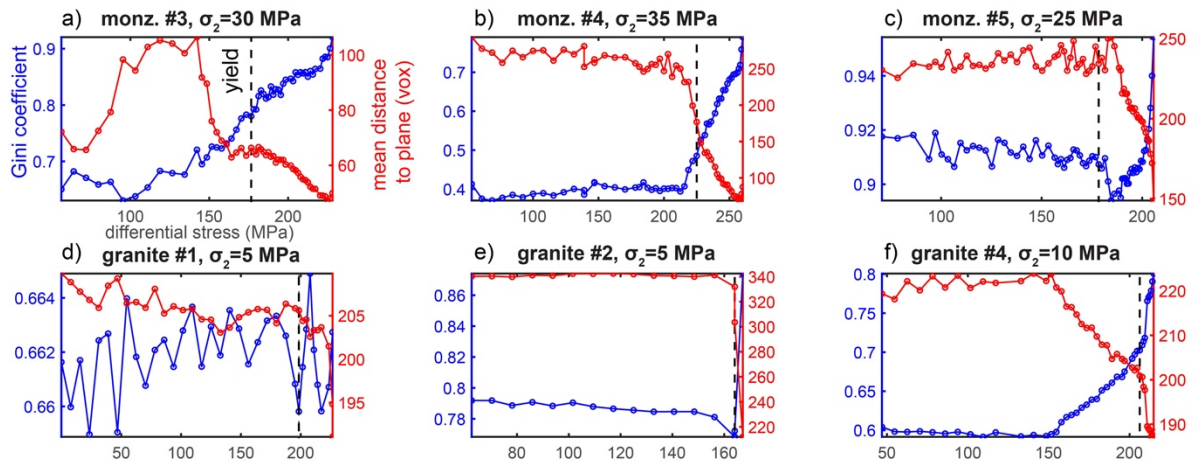
Figure 9. Evolution of the r^2 of the largest fractures and the final failure plane throughout each individual experiment (a-f), and for all the experiments (g). Color of the lines in (g) matches the colors of each experiment shown in (a-f). Triangles show the conditions of the yield point.



724
725
726
727

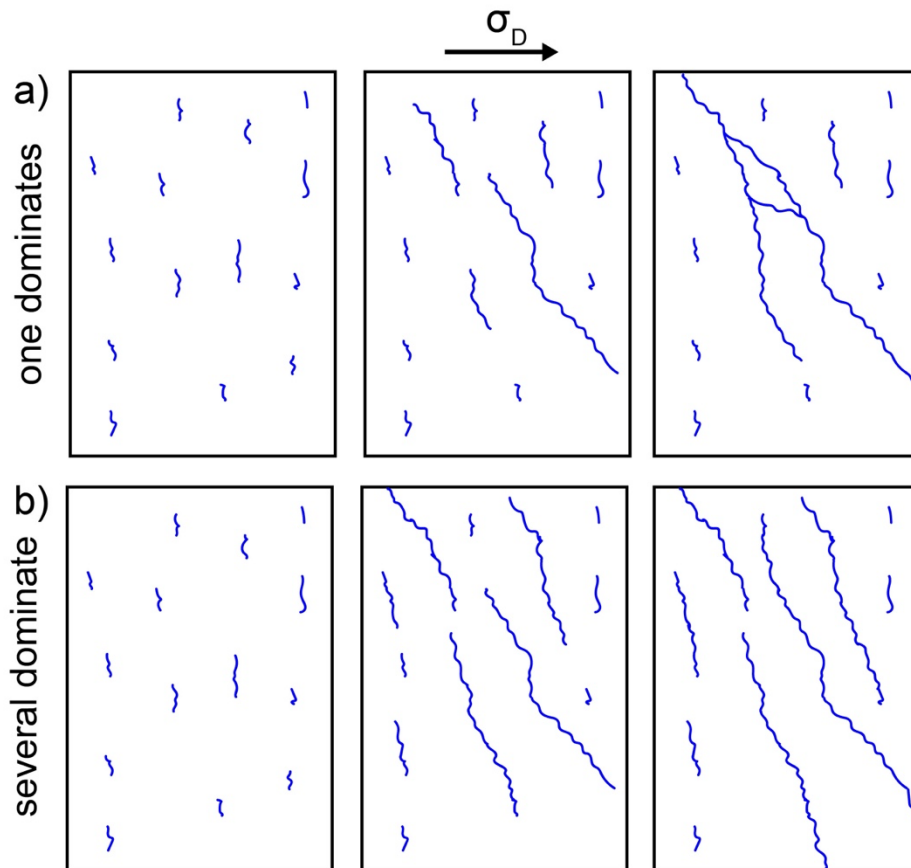
Figure 10. Difference in the r^2 score (a-b), and mean distance between the 10% largest fractures and the failure plane (c-d) from the initial and final tomogram acquired in each experiment. Positive and negative changes from the initial to final scan indicate increasing localization for the r^2 score and mean distance, respectively.

Fracture network localization preceding catastrophic failure



728
729
730
731
732

Figure 11. Evolution of the Gini coefficient and mean distance to the final failure plane in each experiment. Increasing Gini coefficient indicates increasing localization, while decreasing distance indicates increasing localization. Vertical black dashed lines indicate the macroscopic yield point.



733

Figure 12. Fracture network development in a rock in which the one largest fracture dominates development (a) and in which several of the largest fractures dominate (b). The localization observed in experiments monzonite #3 and granite #4 most closely match (a), while the other experiments most closely match (b) (e.g., **Figure 4**).

738

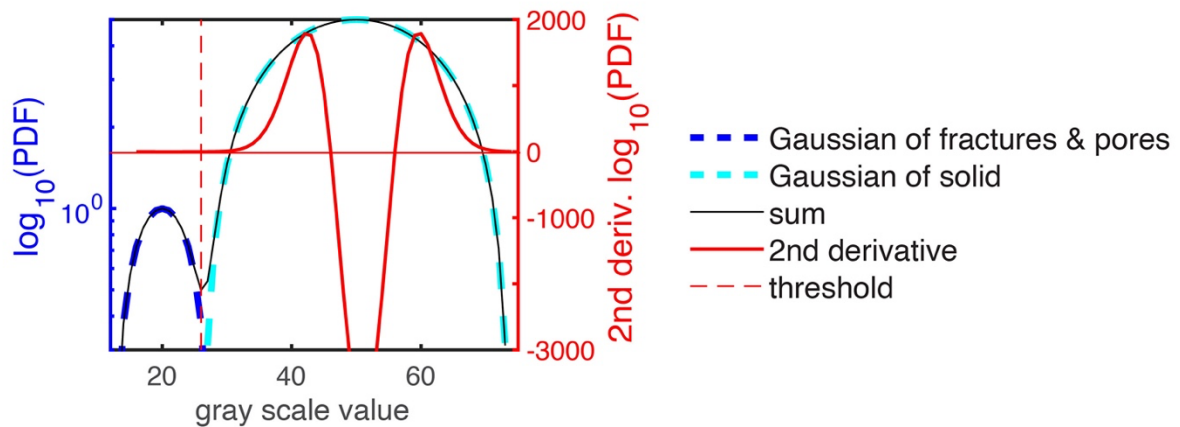
Fracture network localization preceding catastrophic failure

Experiment	Confining stress (MPa)	Pore pressure (MPa)
Monzonite #3	30	0
Monzonite #4	35	5
Monzonite #5	25	0
Granite #1	5	0
Granite #2	5	0
Granite #4	10	0

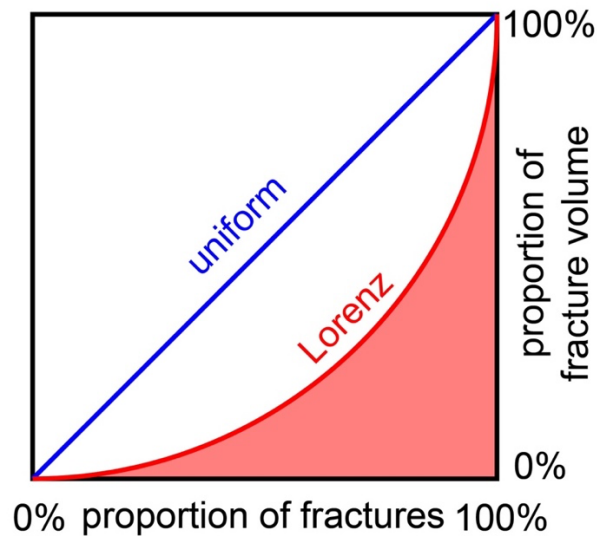
739

740 **Table 1.** Conditions of each experiment.

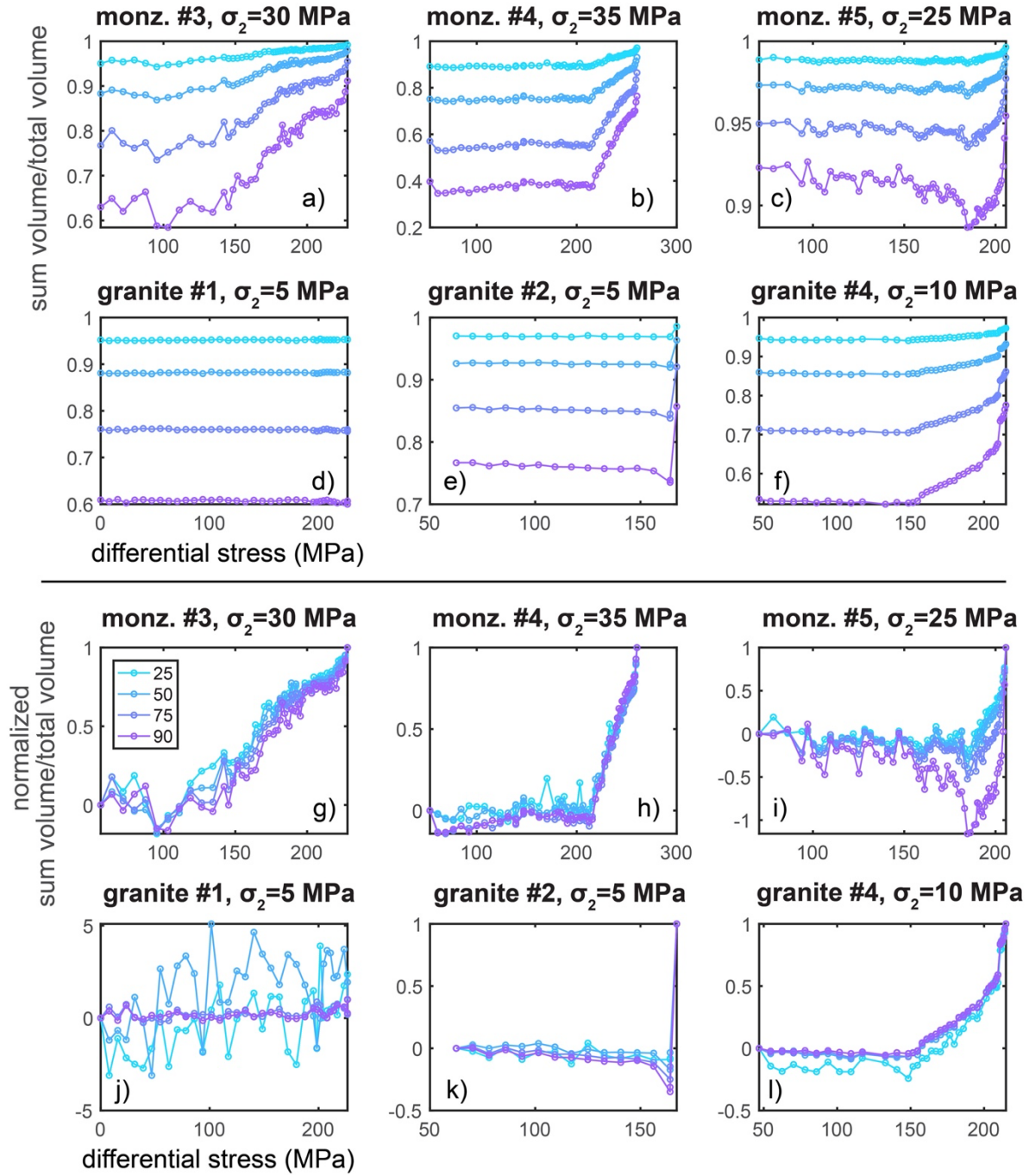
Supplementary Material



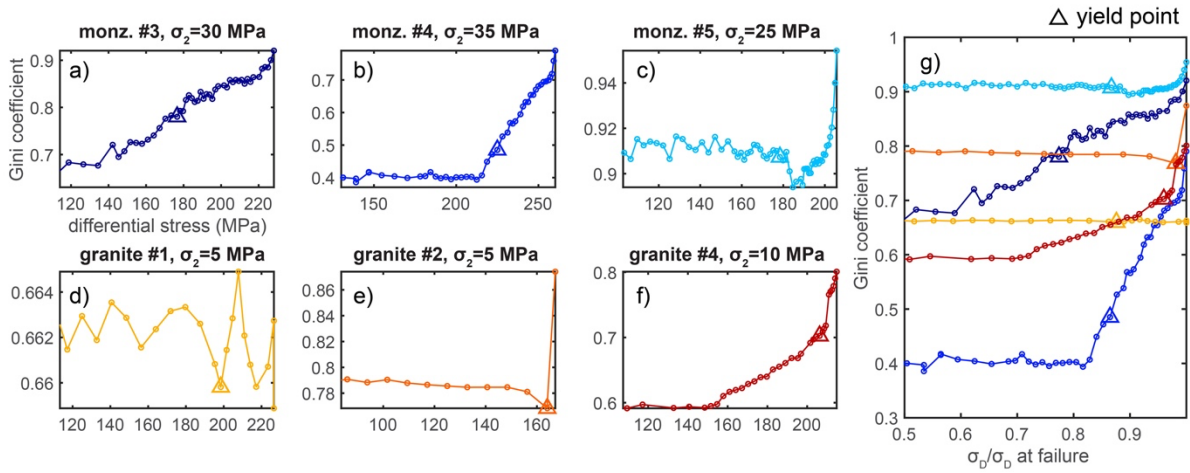
Supplementary Figure 1. Method of selecting the threshold between the solid rock and fractures shown with a synthetic distribution of gray scale values in an X-ray tomogram. First, two fit two Gaussian curves to the two populations of the voids (dark blue) and solid (light blue). Then we calculate the second derivative of the sum of these Gaussian curves (thick red line). Then we find where the second derivative is closest to zero to identify the threshold (dashed red line).



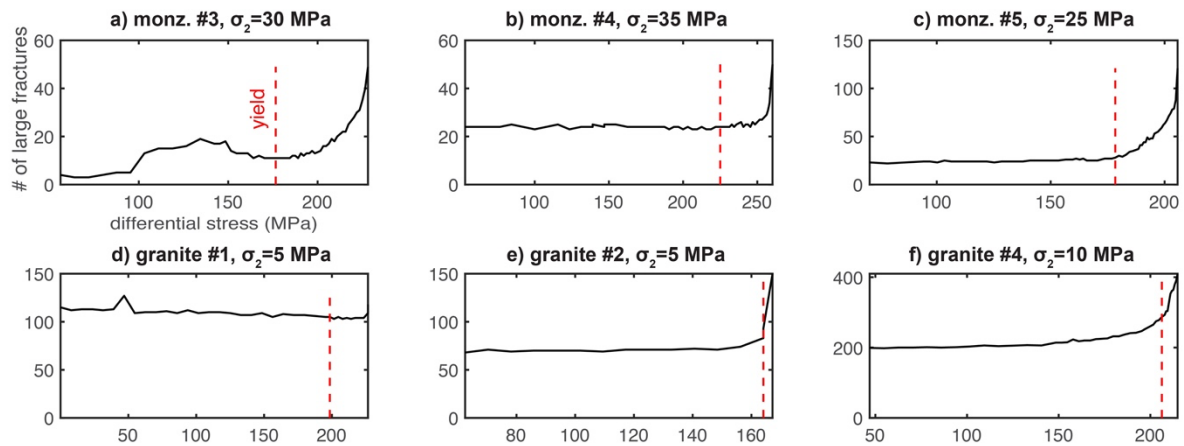
Supplementary Figure 2. The Gini coefficient uses the Lorenz curve of the distribution to measure inequality in a distribution (e.g., *Gini*, 1921). The Lorenz curve shows the proportion of the total amount of a population, such as fracture volume, that is earned by the bottom percentile of a population. The Gini coefficient is one minus twice the integral of the Lorenz curve, shown with the area in red. Thus, larger Gini coefficients indicate that the total volume of all the fractures in a network is dominated by a few fractures, whereas lower Gini coefficients indicate that the total volume is more equally distributed among all the fractures.



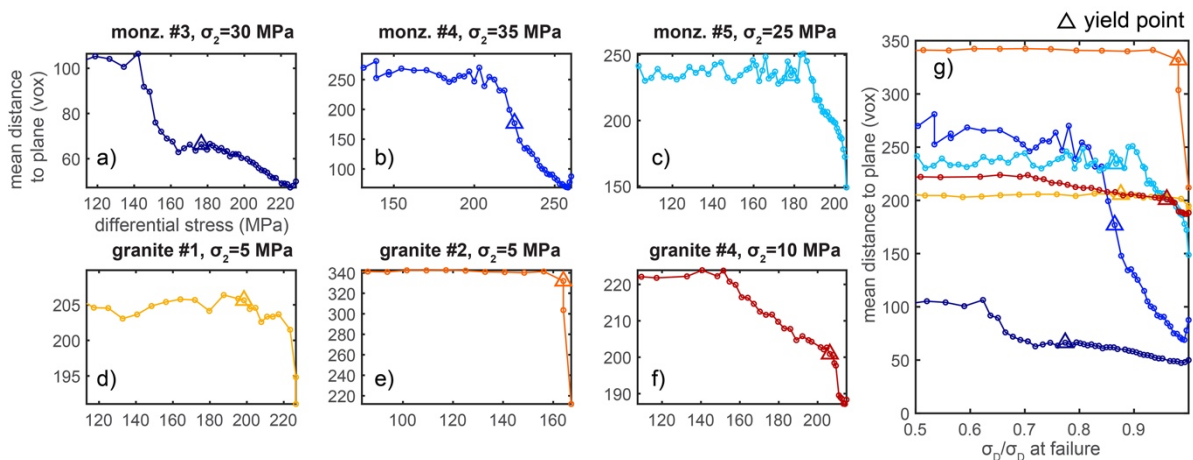
Supplementary Figure 3. Evolution of the sum of the fracture volumes above a range of percentile thresholds unnormalized (a-f) and normalized (g-l) for each experiment. Changing the threshold from the 25th percentile to the 90th percentile decreases the proportion of the sum relative to the total fracture volume, as expected. However, the normalized evolutions show that varying this threshold within this range does not change the general evolution of this metric. In particular, the general conclusion that the sum of the volumes of the largest fractures generally increases toward failure remains unchanged. Note, these evolutions begin to diverge when the threshold is greater than the 90th percentile, i.e., for v_{max}/v_{tot} .



Supplementary Figure 4. Evolution of the Gini coefficient throughout each individual experiment (a-f), and for all the experiments (g). Color of the lines in (g) matches the colors of each experiment shown in (a-f). Triangles show the conditions of the yield point. Increasing Gini coefficient indicates increasing localization toward the largest fractures in the network.



Supplementary Figure 5. Number of fractures in the population with volumes $>90^{\text{th}}$ percentile.



Supplementary Figure 6. Evolution of the mean distance between the top 10^{th} percentile largest fractures and the final failure plane throughout each individual experiment (a-f), and

for all the experiments (g). Color of the lines in (g) matches the colors of each experiment shown in (a-f). Triangles show the conditions of the yield point.